

Combined Spectroscopy and Electrical Characterization of La:BaSnO₃ Thin Films and Heterostructures

Arnaud P. Nono Tchiomo,^{1,2} Emanuela Carleschi,¹ Aletta R. E. Prinsloo,¹ Wilfried Sigle,³ Peter A. van Aken,³ Jochen Mannhart,³ Prosper Ngabonziza,^{1,3, a)} and Bryan P. Doyle^{1, b)}

¹⁾ *Department of Physics, University of Johannesburg, P.O. Box 524 Auckland Park 2006, Johannesburg, South Africa*

²⁾ *Van der Waals-Zeeman Institute, Institute of Physics, Science Park 904, 1098 XH Amsterdam, The Netherlands*

³⁾ *Max Planck Institute for Solid State Research, Heisenbergstr. 1, 70569 Stuttgart, Germany*

(Dated: 29 September 2022)

For La-doped BaSnO₃ thin films grown by pulsed laser deposition, we combine chemical surface characterization and electronic transport studies to probe the evolution of electronic states in the band structure for different La-doping content. Systematic analyses of spectroscopic data based on fitting the core electron line shapes help to unravel the composition of the surface as well as the dynamics associated with increasing doping. This dynamics is observed with a more pronounced signature in the Sn 3d core level, which exhibits an increasing asymmetry to the high binding energy side of the peak with increasing electron density. The present results expand the current understanding of the interplay between the doping concentration, electronic band structure and transport properties of epitaxial La:BaSnO₃ films.

Keywords: XPS, PLD, carrier density, carrier mobility

The perovskite La-doped BaSnO₃ (La:BaSnO₃) is a novel transparent oxide semiconductor that exhibits outstanding room temperature (RT) electron mobility (μ_e) with high carrier density together with a high optical transmittance¹⁻³. Owing to its unique electronic and optical properties, La:BaSnO₃ has the potential for applications in transparent electronics⁴⁻⁷, photovoltaics⁸⁻¹¹, as well as in thermoelectric¹²⁻¹⁵ and multifunctional perovskite-based optoelectronic devices^{10,16,17}. Furthermore, its low-power consumption combined with its ability to be heavily doped and its good stability at high temperatures make La:BaSnO₃ a suitable material for integration in thermally stable capacitors, field effect transistors and power electronic devices^{3,4,17-19}.

The discovery of a RT μ_e of 320 cm² V⁻¹s⁻¹ (with corresponding carrier density, $n = 8 \times 10^{19}$ cm⁻³) in La:BaSnO₃ single crystals¹⁻³ stimulated intense investigation into this material⁴. Particularly, the potential of La:BaSnO₃ for device applications and heterostructures triggered considerable interest in thin films grown from this compound^{5-7,15,17,19-38}. However, the reported μ_e in La:BaSnO₃ thin films have only reached a maximum value of 183 cm² V⁻¹s⁻¹ ($n \simeq 1.2 \times 10^{20}$ cm⁻³) for epitaxial films grown by molecular beam epitaxy (MBE)³³. Other growth techniques resulted in the following electron mobilities: 140 cm² V⁻¹s⁻¹ ($n \simeq 5.2 \times 10^{20}$ cm⁻³) for pulsed laser deposition (PLD)²⁷, 121 cm² V⁻¹s⁻¹ ($n \simeq 4.0 \times 10^{20}$ cm⁻³) for high-pressure magnetron sputtering³⁶, and 53 cm² V⁻¹s⁻¹ ($n \simeq 2.0 \times 10^{20}$ cm⁻³) for chemical solution deposition³⁹. Various strategies

to improve the mobility in La:BaSnO₃ epitaxial films have been explored. Such efforts include, for example, incorporation of undoped BaSnO₃ buffer layers to compensate for the lattice mismatch between the substrate and the active La:BaSnO₃ top layers^{7,19,26,33}, adsorption-controlled MBE for improved stoichiometry control^{31-33,40}, a very high-temperature grown insulating buffer layer to reduce the density of threading dislocations²⁷, and post growth annealing processes^{22,24,41}. Besides the ongoing efforts for RT μ_e improvement, in order to gain a better understanding of the conduction mechanisms in La:BaSnO₃ films, it is important to establish a proper correlation between the transport characteristics and the behavior of the electronic states in the conduction band. This is crucial because the high ambient μ_e in La:BaSnO₃ has been proposed to originate from both the small effective mass of the electrons at the conduction band minimum (CBM)^{25,42}, which is associated with the largely dispersive Sn 5s conduction band, and the low optical phonon scattering rate^{19,43}.

Although several studies used photoemission spectroscopy techniques to investigate the electronic structure of La:BaSnO₃ films^{32,43-46}, only a few reports have combined electronic transport and spectroscopic studies to explore the evolution of electronic states in La:BaSnO₃ films and heterostructures at different La-doping levels^{32,43}. In particular, recent *ex-situ* hard x-ray photoemission spectroscopy (HAXPES) experiments on La:BaSnO₃ films demonstrated that both the CBM and the valence band maximum (VBM), as well as the core electrons are effectively modified with increasing carrier density³². Thus, this result calls for additional combined spectroscopic and electrical characterizations to facilitate more quantitative exploration of the evolution of the intrinsic properties of La:BaSnO₃ films and heterostructures.

^{a)}corresponding author: p.ngabonziza@kf.mpg.de

^{b)}corresponding author: bdoyle@uj.ac.za

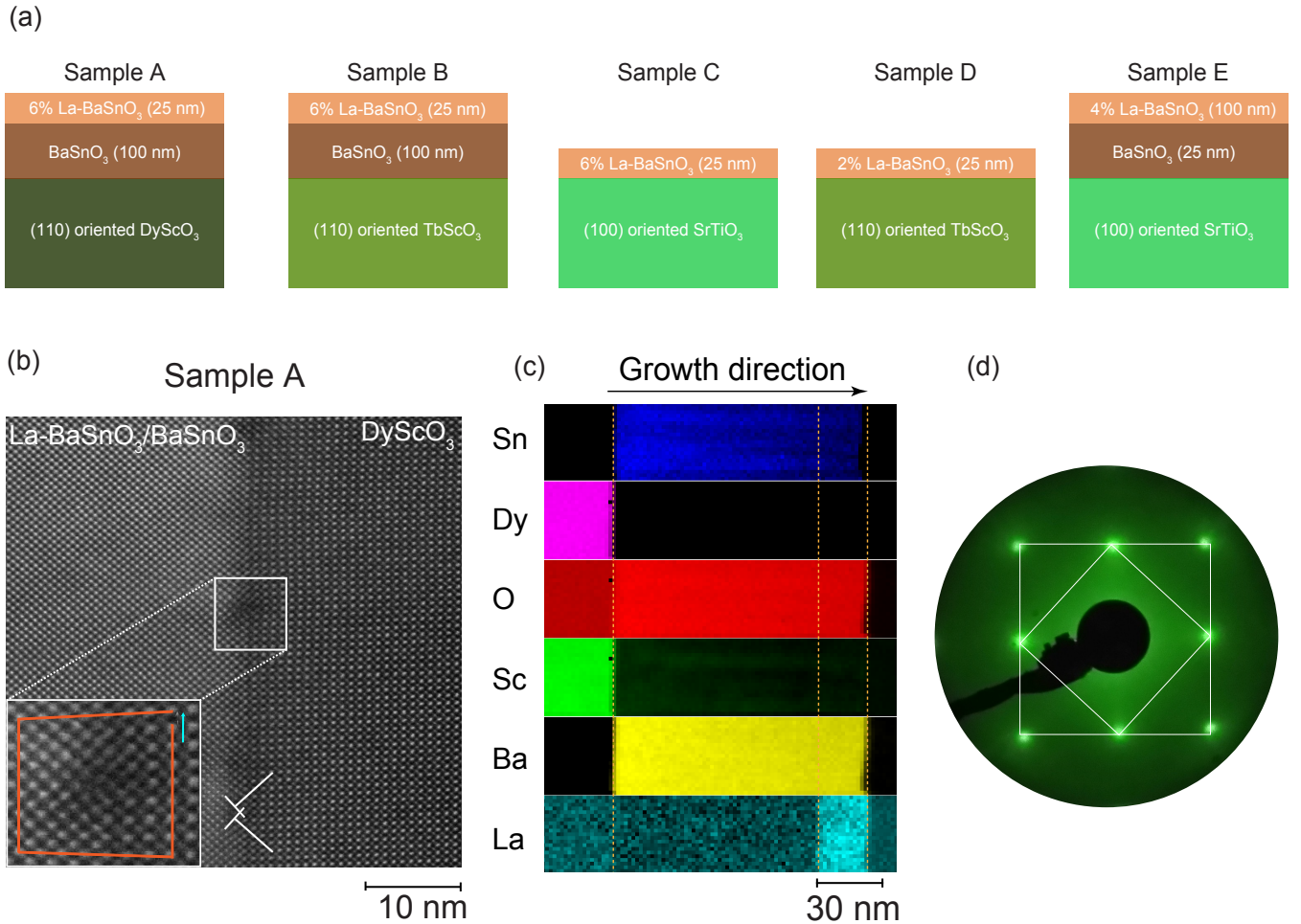


FIG. 1. (a) Schematic layout of the different thin film samples investigated in this study. (b) High-resolution scanning transmission electron microscopy (HRSTEM) image of a representative La:BaSnO₃/BaSnO₃ heterostructure (sample A). Misfit dislocations indicated by the \perp symbols characterize the relaxed interface between the film and the (110) oriented DyScO₃ substrate. The inset represents a high magnification around one of the misfits delimited by the white rectangle, where a lack of closure of the Burgers circuit is seen (orange rectangular-like contour). (c) Electron energy-loss spectroscopy (EELS) elemental mapping for the sample A showing the distribution of the elements in the sample. The signal is divided into regions as indicated by the dashed orange lines. The residual color in the La plot is noise. (d) A representative low energy electron diffraction (LEED) image taken at 48 eV displaying a clean La:BaSnO₃ (001) surface. The diffraction spots form square lattices (white rectangle drawn on the image) in reciprocal space.

tures at different doping levels.

In the present paper we combine chemical surface analysis as a function of La doping using x-ray photoelectron spectroscopy (XPS) and electronic transport studies to explore the evolution of the electronic states in La:BaSnO₃ films and heterostructures. From the transport measurements, we extract the transport characteristics, as well as n and μ_e of the La:BaSnO₃ samples. The surface properties of these samples are subsequently investigated using spectroscopic techniques. A direct connection between the electronic transport characteristics and the spectroscopic data is demonstrated. We used XPS as a probing tool to measure the changes in the films spectra associated with the increasing amount of La³⁺ dopant. Through the analysis and systematic fits

of the core XPS spectra, we are able to extract the binding energy values of the constituent elements along with the associated oxidation states. These data are consistent with the electron energy loss spectroscopy (EELS) data, as well as with the literature. By increasing the doping concentration, we observe shifts of the valence band leading edges toward higher binding energies, as well as increases in the states in the conduction band. More importantly, we provide a quantitative understanding of the effect of conduction band filling in La:BaSnO₃ films and heterostructures. This effect is manifested by an increasing asymmetry in the line shape of the Sn 3d core spectra and leads to considering an additional plasmon satellite peak in the analysis of Sn 3d spectra.

Epitaxial La:BaSnO₃ films and heterostructures (sam-

TABLE I. Electronic transport characteristics (carrier density and mobility) of the samples discussed in this study.

Sample name	Sample layout	Carrier density ($\times 10^{20} \text{ cm}^{-3}$)	Carrier mobility ($\text{cm}^2 \text{ V}^{-1} \text{ s}^{-1}$)
A	6% La:BaSnO ₃ (25 nm)/BaSnO ₃ (100 nm)/DyScO ₃	1.24 ± 0.02	71 ± 2
B	6% La:BaSnO ₃ (25 nm)/BaSnO ₃ (100 nm)/TbScO ₃	4.92 ± 0.05	20 ± 1
C	6% La:BaSnO ₃ (25 nm)/SrTiO ₃	4.05 ± 0.05	91 ± 2
D	2% La:BaSnO ₃ (25 nm)/TbScO ₃	1.35 ± 0.02	75 ± 2
E	4% La:BaSnO ₃ (100 nm)/BaSnO ₃ (25 nm)/SrTiO ₃	0.80 ± 0.05	18 ± 1

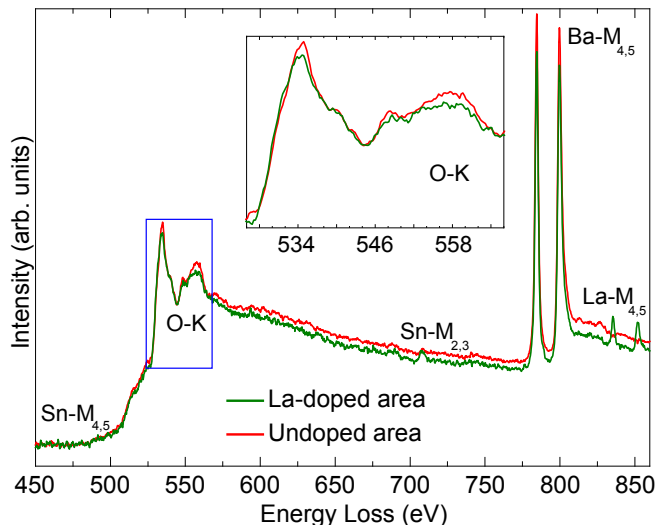


FIG. 2. Electron energy loss spectra of a representative La:BaSnO₃/BaSnO₃ heterostructure. Two regions in the specimen were investigated: an area with only BaSnO₃ (red curve) and another with only La:BaSnO₃ (green curve). The ionized edges of La-M_{4,5}, Ba-M_{4,5} and Sn-M_{4,5} (corresponding to the excitation of 3d states), Sn-M_{2,3} (corresponding to the excitation of 3p states), and O-K (corresponding to the excitation of the 1s state) are resolved. The inset shows the enlargement of the O-K edge delimited by the blue rectangle.

ples labeled A to E in Table I) were prepared by PLD ($\lambda = 248 \text{ nm}$). Prior to deposition, the (100) oriented SrTiO₃, (110) oriented DyScO₃ and TbScO₃ crystalline substrates ($5 \times 5 \times 1 \text{ mm}^3$) were terminated in situ at 1300°C using a CO₂ laser substrate heating system⁴⁷. Figure 1(a) depicts a schematic view of the sample types investigated. The films were grown from La:BaSnO₃ targets of 2%, 4% and 6% La doping contents. Details about the growth and systematic characterization of the films are provided in Ref.²⁷ [see details on the PLD growth conditions in Table S1 of the supplemental information].

Electrical transport properties were measured in a physical property measurement system (PPMS) in a van der Pauw geometry obtained by wire bonding aluminum wires to the samples' corners [see Fig. S1(a) of the supplementary information]. The carrier concentration, n ,

and the electron mobility, μ_e , were determined following the procedure discussed elsewhere^{27,48–50}. Table I gives the carrier density and electron mobility of the different sample types investigated in this study. The La:BaSnO₃ samples analyzed here in both spectroscopy and transport experiments have a RT carrier concentration ranging from $n = 0.80 \times 10^{20}$ to $4.92 \times 10^{20} \text{ cm}^{-3}$; and carrier mobility from $\mu_e = 18$ to $91 \text{ cm}^2 \text{ V}^{-1} \text{ s}^{-1}$. The measured carrier densities reported are smaller than the expected values associated with the nominal concentration of the La dopant. In fact, the doping levels corresponding to 2%, 4% and 6% La are $2.72 \times 10^{20} \text{ cm}^{-3}$, $5.44 \times 10^{20} \text{ cm}^{-3}$ and $8.16 \times 10^{20} \text{ cm}^{-3}$, respectively. The observed discrepancy can be ascribed to the high density of dislocation defects present in the films, as seen in the weak beam dark field scanning transmission electron microscopy micrographs [Fig. S1(b)-(d)]. These defects arise because the films are grown on substrates to which they are poorly lattice matched; and this often results in the reduction of the carrier density and electron mobility in epitaxial La:BaSnO₃ films^{2,27,31,33} [see more details in section S1 of the supplemental information].

Following the procedure described in Ref.⁵¹, the samples were systematically cleaned in ultra-high vacuum (UHV) before photoemission experiments. The surface structure of the samples was characterized using low-energy electron diffraction (LEED) [see Fig. S2(a)-(b) in supplementary information]. The surface of the clean La:BaSnO₃ (001) surface showed a stable 1×1 surface structure [Fig. 1(d)]. The diffraction spots form square lattices in reciprocal space corresponding to the cubic lattice structure of BaSnO₃ in real space, thus indicating the high crystallinity of the films⁵². The cleanliness of the samples was checked by monitoring the LEED patterns directly after an annealing cycle, and also by comparing the XPS survey scans before and after cleaning [see Fig. S2 in supplementary information].

Figure 1(b) shows a representative scanning transmission electron microscopy (STEM) image of the investigated La:BaSnO₃ heterostructure (sample A). To investigate the stoichiometry and evaluate the composition of the epitaxial layers, EELS measurements were performed on the cross section of the samples during STEM characterization. Figure 1(c) displays a representative EELS elemental mapping (atomic layer distribution) of the sam-

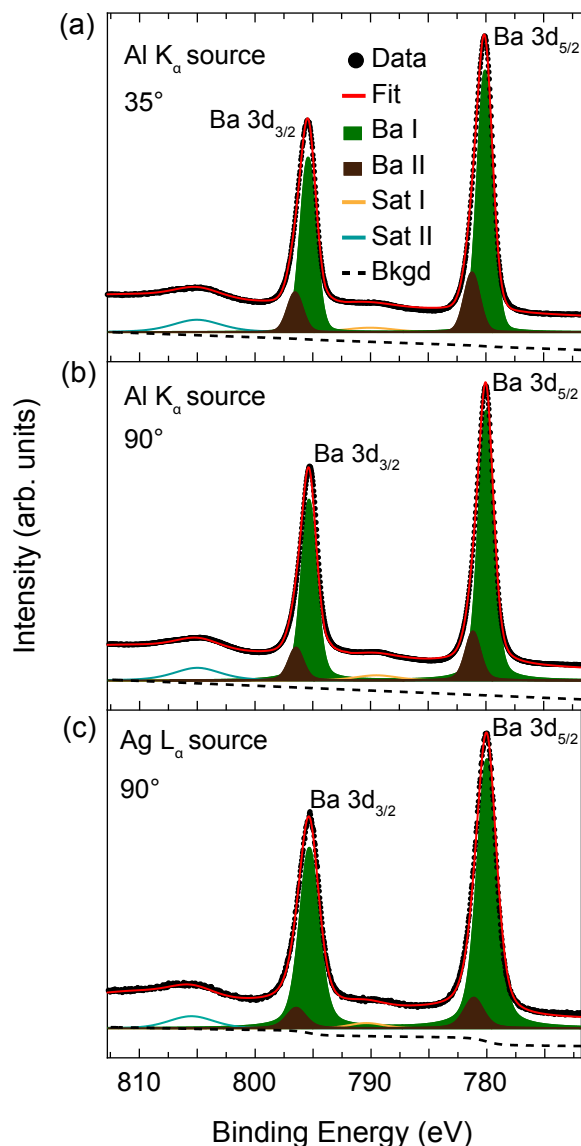


FIG. 3. Angle- and energy-dependent XPS spectra of the Ba 3d core level for the sample B. After subtracting a Shirley background (black dashed lineshape), the Ba 3d core lines are fitted (red lineshape) with two Voigt doublet peaks. The spectra in (a) and (b) were acquired with an Al K_{α} anode (Al K_{α} source) at 35° and 90° take-off angles, respectively. The spectrum in (c) was measured with an Ag L_{α} anode (Ag L_{α} source) at 90° take-off angle. Two satellite features (cyan and orange peaks) are resolved in the spectra. The peak heights were normalized for clarity.

ple A for a total layer thickness of 120 nm of which the La-doped layer is 25 nm thick. The black color suggests a zero intensity, whereas the other colors indicate the presence of different elements (La, Ba, Sn, Dy, Sc, O) that are resolved in the scanned region. The elemental composition of the different layers of the La:BaSnO₃/BaSnO₃ heterostructure is also evidenced in the EELS spectra for the same sample presented in Fig. 2. Looking at all

TABLE II. Surface atomic percentages for the samples measured in XPS.

Sample name	Ba	Sn	O
B	20%	16%	64%
C	25%	15%	60%
D	22%	16%	62%
E	23%	13%	64%

TABLE III. Peak ratios for angle-dependent XPS of the Ba 3d spectra.

	Peak assignment	Peak position (± 0.05 eV)	Relative intensity (± 1 %)	FWHM (± 0.05 eV)
35° Al anode	Ba I	780.08	82	1.58
	Ba II	781.21	18	1.58
90° Al anode	Ba I	780.00	85	1.53
	Ba II	781.13	15	1.53
90° Ag anode	Ba I	780.00	90	1.97
	Ba II	781.13	10	1.97

the ionized edges, it can be seen that the spectra of the BaSnO₃ (red curve) and La:BaSnO₃ (green curve) are very similar, apart from the transfer of spectral weight to the La peaks in the latter. This spectral weight transfer is illustrated by the reduction of the intensity at the Ba-M edge. Intensity reduction is also noticeable at the O-K edge, and could well be due to electronic (charge) modulation associated with the substitution of the bivalent Ba²⁺ atoms with the trivalent La³⁺ ones⁵³. Furthermore, the line shape of the spectra around the O-K feature [see inset Fig. 2] indicate good stoichiometry (no oxygen deficiency) in bulk layers, since these are in good agreement with the O-K EELS spectra reported for stoichiometric BaSnO₃ and La:BaSnO₃ films^{33,54,55}.

Table II presents the elemental composition of the surface of the films obtained from the fit of the XPS spectra. The composition is consistent throughout the surface of the various samples, with a larger proportion of Ba compared to Sn. Most importantly, the oxygen proportion in these high temperature annealed samples demonstrates the stability of the oxygen atoms in La:BaSnO₃^{1,3}, and highlights the robustness of the sample cleaning procedure.

Figure 3 represents the XPS spectra of the Ba 3d core electrons together with the Voigt function fits. The Ba 3d spectra of all the samples showed an asymmetric line shape, suggesting the presence of multiple components in the core level. Two symmetric Voigt doublets (Ba I and Ba II) were used to fit the spectra. The main doublet, Ba I, located at the binding energy of 780.00 eV, is

TABLE IV. Fitted parameters of the Sn 3d regions along with the calculated carrier density in each sample.

Sample name	Peak assignment	Peak position (± 0.05 eV)	FWHM (± 0.05)	Relative intensity ($\pm 1\%$)	Satellite energy (eV)	Carrier density ($\times 10^{20}$ cm $^{-3}$)
E	Screened	486.76	1.07	54	0.30	0.8 ± 0.05
	Unscreened	487.06	1.66	46		
D	Screened	486.51	1.15	52	0.52	1.35 ± 0.02
	Unscreened	487.03	1.34	48		
C	Screened	486.80	1.06	57	0.70	4.05 ± 0.05
	Unscreened	487.50	1.34	43		
B	Screened	486.75	1.12	60	0.80	4.92 ± 0.05
	Unscreened	487.55	1.40	40		

assigned to lattice barium in the Ba $^{2+}$ state, consistent with previous spectroscopic results on powder and epitaxial thin films of BaSnO $_3$ ^{56,57}. The second doublet, Ba II, situated at higher binding energy (781.13 eV), has been attributed to a surface character in several reports on epitaxial BaTiO $_3$ films^{58–60}. This component was suggested to originate either from under-coordinated barium at a BaO terminated surface, or from lattice relaxation^{59,60}.

In comparing the XPS spectra for cleaned surfaces with those of surfaces measured as-inserted [see Figs. S3 and S4 of the supplemental information], the relative intensity of Ba II was observed to decrease after the treatment of the surfaces, while that of Ba I increases. This trend suggests that Ba II could be a surface component, which is amplified with contamination. The nature of the Ba II peak was carefully investigated by carrying out a systematic analysis of its fraction with respect to the probing depth. This was achieved by performing angle-dependent XPS measurements as depicted in Fig. 3. The measurements were first performed using the Al K $_{\alpha}$ anode (photon energy of 1486.71 eV) at electron take-off angles of 35° [Fig. 3(a)] and 90° (normal emission) [Fig. 3(b)], and later the excitation source was changed to Ag L $_{\alpha}$ anode (photon energy of 2984.31 eV) for acquisition at normal emission [Fig. 3(c)]. For the take-off angle of 35°, the photoelectrons emitted originate from a region nearer the surface, whereas at the take-off angle of 90°, the emitted photoelectrons are from a deeper depth within the sample. Hence, the measurement gets more bulk sensitive as the photoelectron take-off angle increases from 35° to 90°, and as the excitation source is changed from Al to Ag. The parameters of the fits pertaining to the angle-dependent analysis are given in Table III. The ratio of the Ba II feature was observed to decrease considerably with bulk sensitivity measurements, thus confirming its surface character.

Two satellite features labeled Sat I and Sat II were also detected in the XPS spectra around the Ba 3d peaks [Fig. 3]. These satellites result from shake-up processes involving Ba 3d photoelectrons and valence electrons^{61,62}. These broad satellites are located about 10 eV

on the high binding energy side of the associated Ba 3d $_{5/2}$ and Ba 3d $_{3/2}$ peaks.

Figure 4 depicts the Sn 3d core level XPS spectra together with the Voigt function fits after subtraction of a Shirley background, for three representative samples of different total carrier density n . The Sn 3d spectral line-shapes display an asymmetry to the high binding energy side of the peak, which increases with increasing carrier density. In metallic systems, the asymmetry in core photoemission spectra arises from intrinsic plasmon excitations associated with the creation of the core hole, which results in an additional component satellite to the main core line^{63,64}. It is known that the Coulomb potential of the core hole creates a localized trap state by capturing a conduction electron^{65–67}. In La:BaSnO $_3$ systems, the conduction band is derived from highly dispersive Sn 5s bands^{32,43}, and the observed doping effect in the Sn 3d core level lineshape is most probably due to screening responses of the conduction electrons introduced by doping⁶³. Therefore, two doublet components were used to fit the Sn 3d spectra assuming that the Koopmans' state (i.e. the excited state after the removal of a core electron from the atom) is projected into screened and unscreened final eigenstates⁶³.

To understand the effect of increasing carrier density in the Sn 3d core level, the spectral lineshape of four samples (B, C, D and E) of different n values were investigated and the analysis results are summarized in Table IV. The core lines were fitted to two Voigt components, which give an excellent description of the overall line shape of the spectra. In each spectrum, the main component is the peak at low binding energy labeled “screened”. This peak has a dominant Gaussian line shape. The component at high binding energy labeled “unscreened” is dominantly Lorentzian, which is a satellite associated with intrinsic plasmon excitations⁶⁷. This peak is broader than the screened component, as evidenced by their FWHM values. Similar satellite structures were reported in the Sn 3d and In 3d core photoemission spectra of binary transparent conducting oxides (Sb-doped SnO $_2$ ^{63,64,68}, In $_2$ O $_3$ –ZnO⁶⁹ and Sn-doped

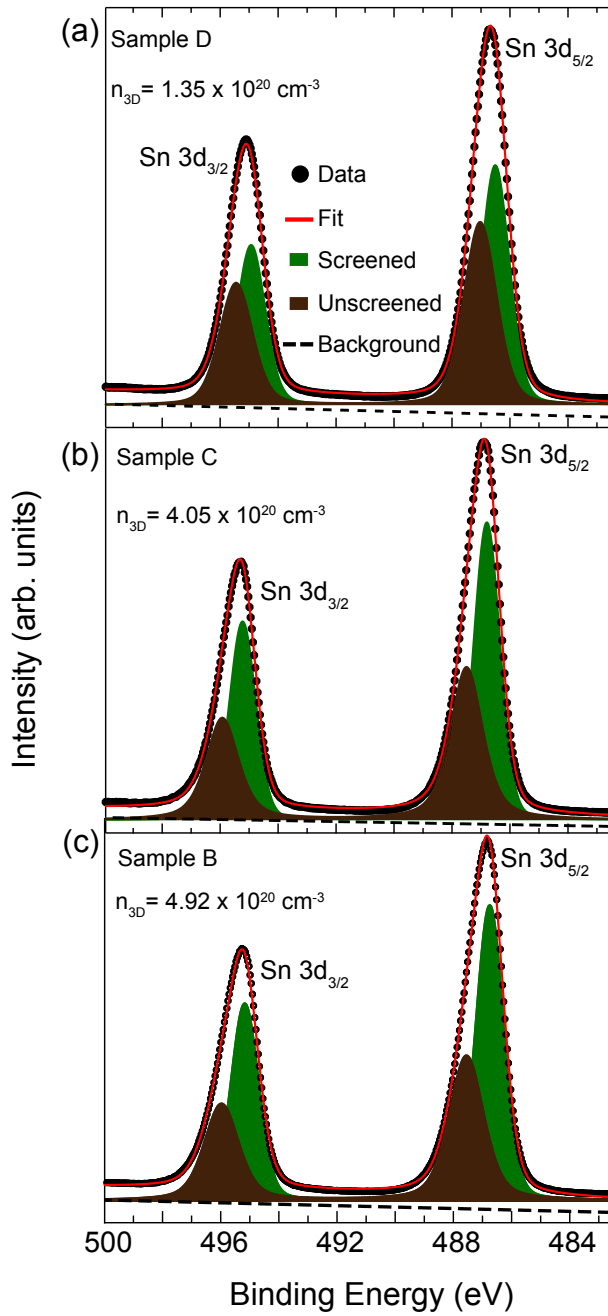


FIG. 4. XPS spectra around the Sn 3d regions for three samples of different total carrier density: (a) Sample D with $n_{3D} = 1.35 \times 10^{20} \text{ cm}^{-3}$, (b) Sample C with $n_{3D} = 4.05 \times 10^{20} \text{ cm}^{-3}$, and (c) Sample B with $n_{3D} = 4.92 \times 10^{20} \text{ cm}^{-3}$. After subtracting a Shirley background (black dashed lineshape), the Sn 3d spectra are fitted (red lineshape) with two Voigt doublet components. The data were acquired at normal emission with the Al K_{α} excitation source.

In_2O_3 ^{67,70}). To better visualize the connection between carrier density and the screened/unscreened intensity and energy, the evolution of both the satellite energy and the intensity of the peaks with $n^{-1/3}$ is plotted [Fig. 5]. As can be seen from Table IV, the binding energy value

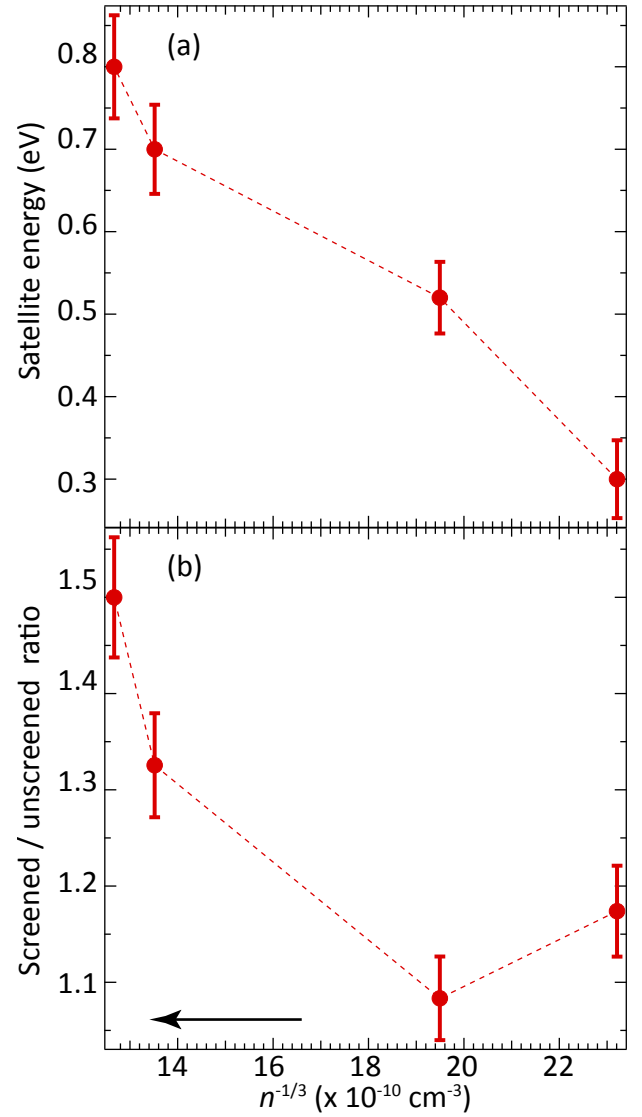


FIG. 5. Variation of the (a) satellite energy and (b) intensity ratio of the screened and unscreened components as a function of $n^{-1/3}$. The error bars in the carrier density are too small to be seen in this plot. The dashed lines are guides to the eye. The black arrow indicates increasing n (plotted data are from Table IV).

of the main component suggests a valence state of 4+ for Sn^{71,72}; and the energy separation (satellite energy) between the main and satellite components increases with n [Fig. 5(a)]. Furthermore, the relative intensity of the screened component increases with increasing n , while that of the unscreened peak decreases. This is indicated in Fig. 5(b) by the increase of the intensity ratio of the peaks, conveying good agreement with previous reports^{64,65,67,69,73}. The discrepancy at the lowest n (sample E) could be ascribed to the fact that the thickness of this sample, 100 nm, surpasses a critical thickness above which additional structural defects are induced in the film^{74,75}. We speculate that defect scattering domi-

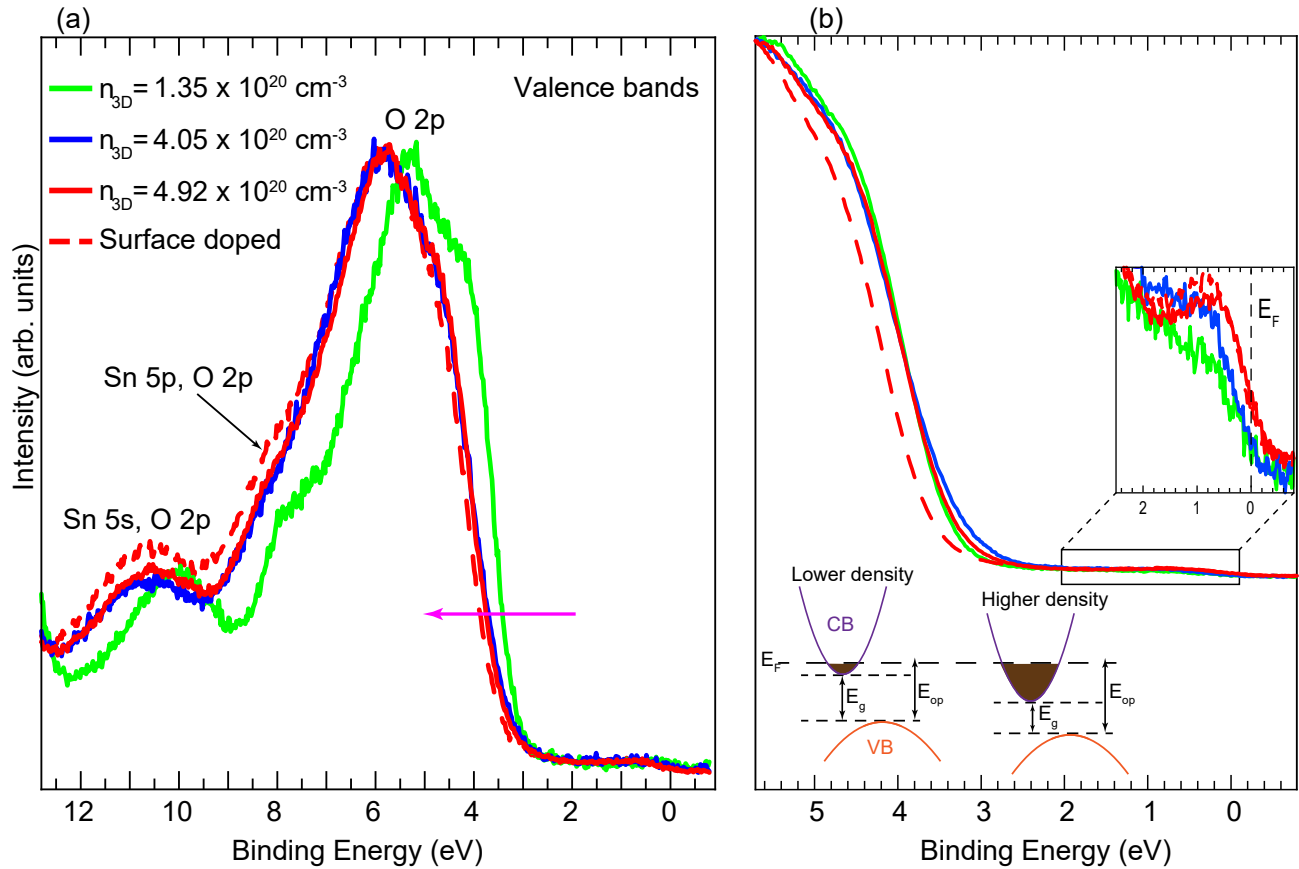


FIG. 6. (a) XPS valence band spectra of three samples of different total carrier density excited with the Al K_{α} anode: Sample D (green curves), Sample C (blue curves), and Sample B (red and red dashed curves). To investigate how surface absorbed carbonate and hydroxide layers affect the states in the valence band region, after initial measurements of the core levels and valence band spectra, the sample B (red dashed curve, surface doped) was intentionally exposed to contamination in the loadlock chamber operated at 1×10^{-8} mbar (not UHV). The carrier densities of all the samples are indicated. The blue, green and red dashed curves are normalized to the maximum intensity of the red curve. The magenta arrow indicates the shift of the valence band with increasing carrier density. (b) Magnified view of the low energy part of the spectra on (a). The bottom left inset is a schematic illustration of the Moss-Burstein shift, which shows how the doping process affects the electronic band structure of the material. The top right inset is enlarged spectra for the region around the Fermi level.

nates, as only 15% of the carriers are activated compared to more than 50% activation for the other samples.

For fitting the spectra, the Gauss-Lorentz ratio was allowed to vary freely. Boundaries were set for the satellite energy. These constraints were applied to the lower limit of the position of the unscreened peak with the consideration that the satellite energy corresponds to the plasmon energy (i.e., the surface plasmon energy) and increases with the carrier density^{63,64,67,76,77}. Since the surface plasmon energy is proportional to the carrier density^{64,70}, the constraints were such that the satellite energy would be in the range of values reported for photoemission spectra of the 3d orbitals in binary transparent conducting oxides^{63,64,67,69} with comparable n values as in samples B, C, D and E. Therefore, the consistent observation of a narrower low binding energy peak and a broader high binding energy peak supports the applicability of the plasmon model to the analysis of the Sn 3d core XPS spectra in these films, which is consistent with previously

reported Sn 3d core level spectra in Sb-doped SnO_2 samples^{63,64,68}.

Next, the effect of increasing carrier density on the valence and conduction band spectra was explored. The same La:BaSnO₃ samples characterized for the core level spectra were used. The XPS spectra of the valence and conduction bands are depicted in Figs. 6(a) and 6(b), respectively.

Three main features are observed in the valence band spectra: (i) a mixture of Sn 5s and bonding O 2p orbitals located at 10.6 eV; (ii) the states at 8.3 eV originating from hybridized Sn 5p and O 2p orbitals; and (iii) the bands at binding energies between 4 and 6 eV associated with O 2p bonding or anti-bonding character^{78–80}. Additionally, shifts of the valence band leading edge to high binding energies upon increasing carrier density can be observed. This indicates an increase in the optical band gap as proposed previously in ellipsometry and HAX-PES results^{25,32,81}. These shifts are correlated to the

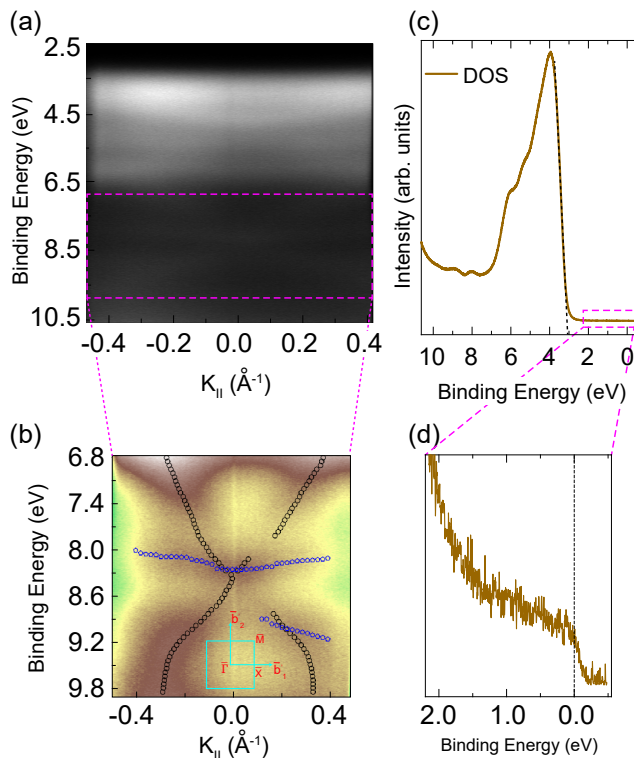


FIG. 7. (a) Representative 2D ARPES map for sample D. The map was acquired in the $\bar{\Gamma} - \bar{X}$ direction. (b) ARPES map of the region indicated by the pink dashed rectangle. The inset shows the first Brillouin zone together with the $\bar{\Gamma}$, \bar{X} and \bar{M} high symmetry points. (c) A representative density of states (DOS) integrated over the entire momentum space from the ARPES map in (a). The black dashed line is a linear extrapolation of the valence band leading edge, revealing that the valence band maximum is located at ~ 3.1 eV. (d) Enlargement of the region around the Fermi level in (c).

shifts observed in the core levels [See section S2 of the supplementary information], as well as to the increasing asymmetry in the Sn 3d core lines. Similar trends were observed in other degenerate doped transparent conducting oxides, which were attributed to the increasing occupation of the states in the conduction band^{63,67,69}. It is noteworthy that an opposite trend (i.e., shift of the valence band spectra toward lower binding energies with increases in La doping) was reported in recent angle resolved photoemission spectroscopy (ARPES) experiments on La:BaSnO₃ films, and it was suggested to originate from the opposite evolution of surface and bulk chemical potentials⁴⁶.

To explore further spectral features arising from occupation of the conduction bands, high resolution scans around the valence band leading edges were acquired [Fig. 6(b)]. To achieve an adequate signal to noise ratio and resolve the fine features in the region close to the Fermi energy (E_F), each spectrum was acquired over a period of about 20 hours. A peak at ~ 4 eV deriving from O 2p orbitals is observed in all spectra as indicated

by their first derivatives [see Fig. S5 of the supplementary information]^{45,46}. For the contaminated surface (sample with the highest n intentionally exposed to contamination in the load lock), a shift to higher binding energy of ~ 0.23 eV is clearly visible in the leading edge valence band spectrum [see red dashed curve in Fig. 6(b)]. Furthermore, a bump is detectable in all spectra in the region between 2 eV and E_F [see top right inset in Fig. 6(b)]. The spectra exhibit a weak structure close to E_F , which terminates in a sharp Fermi edge. This structure is associated with occupied states in the conduction band (Sn 5s orbital character with a small contribution from O 2p orbitals)^{32,43}. Moreover, the intensity of this CBM peak is observed to increase in the contaminated surface as evidenced by the red dashed curve [see top right inset in Fig. 6(b)]. This suggests that exposure of the surface to contamination results in increasing occupied states in the conduction band. We attribute this behavior to the Moss-Burstein effect, i.e., the apparent optical band gap of the material is increased as the absorption edge is pushed to higher energies as a result of some states close to the conduction band being populated [see, bottom left inset in Fig. 6(b)]^{82,83}. Indeed, the valence band shifts associated with the increasing density of electrons occupying the conduction band were reported in several transparent conducting oxides, resulting in the increase of the intensity of the conduction band feature^{25,32,67,69,84}.

To date, few ARPES studies of the electronic band structure of La:BaSnO₃ and BaSnO₃ films have been reported⁴⁴⁻⁴⁶. In Fig. 7, we present the ARPES data of the band structure of a representative La:BaSnO₃ film (Sample D) exposed to air for days before cleaning in vacuum⁸⁵. These data were collected at room temperature. Although ARPES is a very surface sensitive technique and the samples were exposed to ambient conditions, valence band dispersion is observed from about 3.10 to 10.62 eV [Fig. 7(a)]. The fact that these bands are not clearly resolved is understood in terms of the need for a very particular surface treatment associated with *ex-situ* ARPES measurements⁴⁴. Figure 7(b) depicts a high-resolution 2D ARPES map in the binding energies ranging from 6.8 to ~ 9.8 eV around the hybridized Sn 5s and O 2p states. Some highly dispersive bands are resolved: the black markers overlaying the dispersing bands are extracted band dispersions obtained from peak fitting of the momentum distribution curves (MDCs), whereas the blue markers are for bands fitted to peaks in the energy distribution curves (EDCs). Figure 7(c) represents the density of states (DOS) integrated from the ARPES map (i.e., EDC obtained from the ARPES map over the entire momentum space). The DOS spectrum exhibits well resolved band features that are similar to the XPS valence band spectra [Fig. 6(a)]. The Fermi-Dirac edge straddling 0 eV is visible [Fig. 7(d)], and a linear extrapolation of the valence band leading edge reveals that the VBM is situated at ~ 3.1 eV [see, black dashed line in Fig. 7(c)]. The extracted VBM value is in close agreement to previous theoretical and experi-

mental values^{43–46}. For this sample investigated in both XPS and ARPES, the same value for the VBM is obtained from both techniques; and the CBM is not well developed as evidenced by the data for both techniques shown in the insets in Fig. 6b and Fig. 7d.

In summary, we have systematically investigated the evolution of electronic states in the band structure of La:BaSnO₃ films at different La doping levels. A close connection between the transport and the spectroscopic characteristics is demonstrated. In particular, increasing the carrier concentration in the conduction band by doping is observed to significantly affect the core and valence band spectra. The Sn 3d core line shape presents a pronounced asymmetry variation with the carrier density, and is fitted following the plasmon model applicable to metallic systems. Scans around the valence band spectra allowed the detection of the occupied states in the conduction bands. It is determined that surface contamination could potentially induce surface carrier accumulation, supported by the increase in the intensity of the CBM detected in the surface exposed to contamination. This study presents a detailed characterization of the chemical composition of the near-surface region of La:BaSnO₃, and it provides a better picture of the interplay between the doping concentration, electronic band structure and transport properties of epitaxial La:BaSnO₃ films. The ARPES data presented in this study highlight the challenge of surface preparation for ex-situ ARPES measurements of epitaxial La:BaSnO₃ films and heterostructures. Preferably, a portable vacuum suitcase is ideal for long-distance transport of epitaxial La:BaSnO₃ films in UHV conditions to perform further in situ ARPES analysis at different locations⁸⁶ and/or development of protective capping methods for in situ capping to avoid any possible surface contamination when films are exposed to ambient conditions.

Supplementary Material

See supplementary material for details on electronic transport measurements, additional microstructural and photoemission spectroscopy characterizations of La:BaSnO₃ films and heterostructures.

The authors gratefully acknowledge fruitful discussions and technical support by Kathrin Küster. B. P. Doyle, A. P. Nono Tchiomo, A. R. E. Prinsloo and E. Carleschi acknowledge funding support from the National Research Foundation (NRF) of South Africa under Grant Nos. 93205, 90698, 99030, and 111985. W. Sigle and P. van Aken acknowledge funding from the European Union's Horizon 2020 research and innovation programme under grant agreement No. 823717-ESTEEM3.

REFERENCES

¹H. J. Kim, U. Kim, H. M. Kim, T. H. Kim, H. S. Mun, B.-G. Jeon, K. T. Hong, W.-J. Lee, C. Ju, K. H. Kim, and K. Char, *Appl. Phys. Express* **5**, 061102 (2012).

²H. J. Kim, U. Kim, T. H. Kim, J. Kim, H. M. Kim, B.-G. Jeon, W.-J. Lee, H. S. Mun, K. T. Hong, J. Yu, K. Char, and K. H. Kim, *Phys. Rev. B* **86**, 165205 (2012).

³X. Luo, Y. S. Oh, A. Sirenko, P. Gao, T. A. Tyson, K. Char, and S.-W. Cheong, *Appl. Phys. Lett.* **100**, 172112 (2012).

⁴W.-J. Lee, H. J. Kim, J. Kang, D. H. Jang, T. H. Kim, J. H. Lee, and K. H. Kim, *Annu. Rev. Mater. Res.* **47**, 391 (2017), and references therein.

⁵U. Kim, C. Park, T. Ha, Y. M. Kim, N. Kim, C. Ju, J. Park, J. Yu, J. H. Kim, and K. Char, *APL Mater.* **3**, 036101 (2015).

⁶J. Yue, A. Prakash, M. C. Robbins, S. J. Koester, and B. Jalan, *ACS Appl. Mater. Interfaces* **10**, 21061 (2018).

⁷Z. Wang, H. Paik, Z. Chen, D. A. Muller, and D. G. Schlom, *APL Mater.* **7**, 022520 (2019).

⁸Y. Zhang, M. P. K. Sahoo, and J. Wang, *Phys. Chem. Chem. Phys.* **19**, 7032 (2017).

⁹S. S. Shin, J. S. Kim, J. H. Suk, K. D. Lee, D. W. Kim, J. H. Park, I. S. Cho, K. S. Hong, and J. Y. Kim, *ACS Nano* **7**, 1027 (2013).

¹⁰J. Park, U. Kim, and K. Char, *Appl. Phys. Lett.* **108**, 092106 (2016).

¹¹E. Fortunato, D. Ginley, H. Hosono, and D. C. Paine, *MRS Bulletin* **32**, 2007 (2016).

¹²J. Li, Z. Ma, R. Sa, and K. Wu, *RSC Adv.* **7**, 32703 (2017).

¹³P. Rajasekaran, M. Arivanandhan, Y. Kumaki, R. Jayavel, Y. Hayakawa, and M. Shimomura, *CrystEngComm.* **22**, 5363 (2020).

¹⁴T. Wu and P. Gao, *Materials* **11**, 999 (2018).

¹⁵H. J. Cho, B. Feng, T. Onozato, M. Wei, A. V. Sanchela, Y. Ikuhara, and H. Ohta, *Phys. Rev. Materials* **3**, 094601 (2019).

¹⁶S. Ismail-Beigi, F. J. Walker, S.-W. Cheong, K. M. Rabe, and C. H. Ahn, *APL Materials* **3**, 062510 (2015).

¹⁷K. Krishnaswamy, L. Bjaalie, B. Himmetoglu, A. Janotti, L. Gordon, and C. G. Van de Walle, *Appl. Phys. Lett.* **108**, 083501 (2016).

¹⁸D. S. Ginley and C. Bright, *MRS Bulletin* **25**, 15 (2000).

¹⁹A. Prakash, P. Xu, A. Faghaninia, S. Shukla, J. W. Ager, C. S. Lo, and B. Jalan, *Nat. Commun.* **8**, 15167 (2017).

²⁰U. S. Alaam, F. J. Wong, J. J. Ditto, A. W. Robertson, E. Lindgren, A. Prakash, G. Haugstad, P. Shafer, A. T. N'Diaye, D. Johnson, E. Arenholz, B. Jalan, N. D. Browning, and Y. Suzuki, *Phys. Rev. Materials* **3**, 124402 (2019).

²¹A. V. Sanchela, M. Wei, H. Zensyo, B. Feng, J. Lee, G. Kim, H. Jeon, Y. Ikuhara, and H. Ohta, *Appl. Phys. Lett.* **112**, 232102 (2018).

²²H. J. Cho, T. Onozato, M. Wei, A. Sanchela, and H. Ohta, *APL Mater.* **7**, 022507 (2019).

²³S. Yu, D. Yoon, and J. Son, *Appl. Phys. Lett.* **108**, 262101 (2016).

²⁴D. Yoon, S. Yu, and J. Son, *NPG Asia Mater.* **10**, 363 (2018).

²⁵C. A. Niedermeier, S. Rhode, K. Ide, H. Hiramatsu, H. Hosono, T. Kamiya, and M. A. Moram, *Phys. Rev. B* **95**, 161202 (2017).

²⁶P. V. Wadekar, J. Alaria, M. O'Sullivan, N. L. O. Flack, T. D. Manning, L. J. Phillips, K. Durose, O. Lozano, S. Lucas, J. B. Claridge, and M. J. Rosseinsky, *Appl. Phys. Lett.* **105**, 052104 (2014).

²⁷A. P. Nono Tchiomo, W. Braun, B. P. Doyle, W. Sigle, P. van Aken, J. Mannhart, and P. Ngabonziza, *APL Mater.* **7**, 041119 (2019).

²⁸F.-Y. Fan, W.-Y. Zhao, T.-W. Chen, J.-M. Yan, J.-P. Ma, L. Guo, G.-Y. Gao, F.-F. Wang, and R.-K. Zheng, *Appl. Phys. Lett.* **113**, 202102 (2018).

²⁹H. Mizoguchi, P. Chen, P. Boolchand, V. Ksenofontov, C. Felser, P. W. Barnes, and P. M. Woodward, *Chem. Mater.* **25**, 3858 (2013).

³⁰K. Fujiwara, K. Nishihara, J. Shiogai, and A. Tsukazaki, *Appl. Phys. Lett.* **110**, 203503 (2017).

³¹S. Raghavan, T. Schumann, H. Kim, J. Y. Zhang, T. A. Cain, and S. Stemmer, *APL Mater.* **4**, 016106 (2016).

³²Z. Lebens-Higgins, D. O. Scanlon, H. Paik, S. Sallis, Y. Nie, M. Uchida, N. F. Quackenbush, M. J. Wahila, G. E. Sterbinsky,

- D. A. Arena, J. C. Woicik, D. G. Schlom, and L. F. J. Piper, *Phys. Rev. Lett.* **116**, 027602 (2016).
- ³³H. Paik, Z. Chen, E. Lochocki, A. Seidner H., A. Verma, N. Tanen, J. Park, M. Uchida, S. Shang, B.-C. Zhou, M. Brützmam, R. Uecker, Z.-K. Liu, D. Jena, K. M. Shen, D. A. Muller, and D. G. Schlom, *APL Mater.* **5**, 116107 (2017).
- ³⁴H. Wang, A. Prakash, K. Reich, K. Ganguly, B. Jalan, and C. Leighton, *APL Mater.* **8**, 071113 (2020).
- ³⁵W. M. Postiglione, K. Ganguly, H. Yun, J. S. Jeong, A. Jacobson, L. Borgeson, B. Jalan, K. A. Mkhoyan, and C. Leighton, *Phys. Rev. Materials* **5**, 044604 (2021).
- ³⁶R. Zhang, X. Li, J. Bi, S. Zhang, S. Peng, Y. Song, Q. Zhang, L. Gu, J. Duan, and Y. Cao, *APL Mater.* **9**, 061103 (2021).
- ³⁷K. Ganguly, A. Prakash, B. Jalan, and C. Leighton, *APL Mater.* **5**, 056102 (2017).
- ³⁸K. Ganguly, P. Ambwani, P. Xu, J. S. Jeong, K. A. Mkhoyan, C. Leighton, and B. Jalan, *APL Mater.* **3**, 062509 (2015).
- ³⁹Y. He, R. Wei, C. Zhou, W. Cheng, X. Ding, C. Shao, L. Hu, W. Song, X. Zhu, and Y. Sun, *Cryst. Growth Des.* **21**, 5800 (2021).
- ⁴⁰A. Prakash, P. Xu, X. Wu, G. Haugstad, X. Wang, and B. Jalan, *J. Mater. Chem. C* **5**, 5730 (2017).
- ⁴¹W.-J. Lee, H. J. Kim, E. Sohn, T. H. Kim, J.-Y. Park, W. Park, H. Jeong, T. Lee, J. H. Kim, K.-Y. Choi, and K. H. Kim, *Appl. Phys. Lett.* **108**, 082105 (2016).
- ⁴²D. O. Scanlon, *Phys. Rev. B* **87**, 161201 (2013).
- ⁴³S. Sallis, D. O. Scanlon, S. C. Chae, N. F. Quackenbush, D. A. Fischer, J. C. Woicik, J.-H. Guo, S. W. Cheong, and L. F. J. Piper, *Appl. Phys. Lett.* **103**, 042105 (2013).
- ⁴⁴S. Soltani, S. Hong, B. Kim, D. Kim, J. K. Jung, B. Sohn, T. W. Noh, K. Char, and C. Kim, *Phys. Rev. Materials* **4**, 055003 (2020).
- ⁴⁵B. S. Joo, Y. J. Chang, L. Moreschini, A. Bostwick, E. Rotenberg, and M. Han, *Curr. Appl. Phys.* **17**, 595 (2017).
- ⁴⁶E. B. Lochocki, H. Paik, M. Uchida, D. G. Schlom, and K. M. Shen, *Appl. Phys. Lett.* **112**, 181603 (2018).
- ⁴⁷W. Braun, M. Jäger, G. Laskin, P. Ngabonziza, W. Voesch, P. Wittlich, and J. Mannhart, *APL Mater.* **8**, 071112 (2020).
- ⁴⁸P. Ngabonziza, M. P. Stehno, H. Myoren, V. A. Neumann, G. Koster, and A. Brinkman, *Adv. Electron. Mater.* **2**, 1600157 (2016).
- ⁴⁹P. Ngabonziza, Y. Wang, and A. Brinkman, *Phys. Rev. Materials* **2**, 044204 (2018).
- ⁵⁰P. Ngabonziza, *Nanotechnology* **33**, 192001 (2022).
- ⁵¹A. P. Nono Tchiomo, G. Babu-Geetha, E. Carleschi, P. Ngabonziza, and B. P. Doyle, *Surf. Sci. Spectra* **25**, 024001 (2018).
- ⁵²M. A. V. Hove and S. Y. Tong, *Surface crystallography by LEED: theory, computation and structural results*, (Springer, Berlin, 1979).
- ⁵³Y. Liu, H. Huang, L. Xue, J. Sun, X. Wang, P. Xiong, and J. Zhu, *Nanoscale* **13**, 19840 (2021).
- ⁵⁴W. Y. Wang, Y. L. Tang, Y. L. Zhu, J. Suriyaprakash, Y. B. Xu, Y. Liu, B. Gao, S.-W. Cheong, and X. L. Ma, *Sci. Rep.* **5**, 16097 (2015).
- ⁵⁵H. Yun, M. Topsakal, A. Prakash, K. Ganguly, C. Leighton, B. Jalan, R. M. Wentzcovitch, K. A. Mkhoyan, and J. S. Jeong, *J. Vac. Sci. Technol.* **36**, 031503 (2018).
- ⁵⁶G. Larramona, C. Gutiérrez, I. Pereira, M. R. Nunes, and F. M. A. da Costa, *J. Chem. Soc. Faraday Trans. 1* **85**, 907 (1989).
- ⁵⁷H. M. I. Jaim, S. Lee, X. Zhang, and I. Takeuchi, *Appl. Phys. Lett.* **111**, 172102 (2017).
- ⁵⁸J. E. Rault, G. Agnus, T. Maroutian, V. Pillard, P. Lecoeur, G. Niu, B. Vilquin, M. G. Silly, A. Bendouan, F. Sirotti, and N. Barrett, *Phys. Rev. B* **87**, 155146 (2013).
- ⁵⁹X. L. Li, B. Chen, H. Y. Jing, H. B. Lu, B. R. Zhao, Z. H. Mai, and Q. J. Jia, *Appl. Phys. Lett.* **87**, 222905 (2005).
- ⁶⁰X. L. Li, H. B. Lu, M. Li, Z. Mai, H. Kim, and Q. J. Jia, *Appl. Phys. Lett.* **92**, 012902 (2008).
- ⁶¹J. A. Colón Santana, *Quantitative Core Level Photoelectron Spectroscopy* (Morgan & Claypool Publishers, San Rafael, USA, 2015).
- ⁶²G. B. Armen, T. Åberg, K. R. Karim, J. C. Levin, B. Crasemann, G. S. Brown, M. H. Chen, and G. E. Ice, *Phys. Rev. Lett.* **54**, 182 (1985).
- ⁶³R. G. Egdell, J. Rebane, T. J. Walker, and D. S. L. Law, *Phys. Rev. B* **59**, 179 (1999).
- ⁶⁴R. Egdell, T. Walker, and G. Beamson, *J. Electron Spectrosc. Relat. Phenom.* **128**, 59 (2003).
- ⁶⁵J. N. Chazalviel, M. Campagna, G. K. Wertheim, and H. R. Shanks, *Phys. Rev. B* **16**, 697 (1977).
- ⁶⁶M. Campagna, G. K. Wertheim, H. R. Shanks, F. Zumsteg, and E. Banks, *Phys. Rev. Lett.* **34**, 738 (1975).
- ⁶⁷C. Körber, V. Krishnakumar, A. Klein, G. Panaccione, P. Torelli, A. Walsh, J. L. F. Da Silva, S.-H. Wei, R. G. Egdell, and D. J. Payne, *Phys. Rev. B* **81**, 165207 (2010).
- ⁶⁸P. Cox, R. Egdell, C. Harding, A. Orchard, W. Patterson, and P. Tavener, *Solid State Commun.* **44**, 837 (1982).
- ⁶⁹J. Jia, N. Oka, and Y. Shigesato, *J. Appl. Phys.* **113**, 163702 (2013).
- ⁷⁰V. Christou, M. Etchells, O. Renault, P. J. Dobson, O. V. Salata, G. Beamson, and R. G. Egdell, *J. Appl. Phys.* **88**, 5180 (2000).
- ⁷¹W. E. Morgan and J. R. Van Wazer, *J. Phys. Chem.* **77**, 964 (1973).
- ⁷²V. B. Crist, *Handbook of monochromatic XPS spectra: The elements of native oxides* (John Wiley & Sons, Chichester, 2000).
- ⁷³D. C. Langreth, Theory of plasmon effects in high-energy spectroscopy, in *Proceedings of Nobel Symposium 24 in Medicine and Natural Science*, edited by B. Lundqvist and S. Lundqvist (Academic Press, New York and London, 1973) pp. 210–222.
- ⁷⁴P. R. Berger, K. Chang, P. Bhattacharya, J. Singh, and K. Bajaj, *Appl. Phys. Lett.* **53**, 684 (1988).
- ⁷⁵M. Kneiß, P. Storm, A. Hassa, D. Splith, H. von Wenckstern, M. Lorenz, and M. Grundmann, *APL Mater.* **8**, 051112 (2020).
- ⁷⁶D. J. Payne, R. G. Egdell, W. Hao, J. S. Foord, A. Walsh, and G. W. Watson, *Chem. Phys. Lett.* **411**, 181 (2005).
- ⁷⁷P.-A. Glans, T. Learmonth, K. E. Smith, J. Guo, A. Walsh, G. W. Watson, F. Terzi, and R. G. Egdell, *Phys. Rev. B* **71**, 235109 (2005).
- ⁷⁸J. M. Themlin, R. Sporcken, J. Darville, R. Caudano, J. M. Gilles, and R. L. Johnson, *Phys. Rev. B* **42**, 11914 (1990).
- ⁷⁹S. K. Vasheghani Farahani, T. D. Veal, J. J. Mudd, D. O. Scanlon, G. W. Watson, O. Bierwagen, M. E. White, J. S. Speck, and C. F. McConville, *Phys. Rev. B* **90**, 155413 (2014).
- ⁸⁰L. Kövér, G. Moretti, Z. Kovács, R. Sanjinés, I. Cserny, G. Margaritondo, J. Pálinkás, and H. Adachi, *J. Vac. Sci. Technol. A* **13**, 1382 (1995).
- ⁸¹D. Seo, K. Yu, Y. Jun Chang, E. Sohn, K. Hoon Kim, and E. J. Choi, *Appl. Phys. Lett.* **104**, 022102 (2014).
- ⁸²E. Burstein, *Phys. Rev.* **93**, 632 (1954).
- ⁸³T. S. Moss, *Proc. Phys. Soc. B* **67**, 775 (1954).
- ⁸⁴J. J. Mudd, T.-L. Lee, V. Muñoz Sanjosé, J. Zúñiga Pérez, D. J. Payne, R. G. Egdell, and C. F. McConville, *Phys. Rev. B* **89**, 165305 (2014).
- ⁸⁵The La:BaSnO₃ films were prepared at the Max Planck Institute for Solid State Research, Stuttgart, Germany and transported at ambient conditions for further spectroscopic measurements (XPS and ARPES) to the University of Johannesburg, South Africa. Details on the cleaning procedure of the samples and spectroscopic measurements are presented in supplementary information.
- ⁸⁶P. Ngabonziza, M. P. Stehno, G. Koster, and A. Brinkman, In Situ Characterization Tools for Bi₂Te₃ Topological Insulator Nanomaterials, in *In-situ Characterization Techniques for Nanomaterials*, edited by C. S. Kumar (Springer Berlin Heidelberg, 2018) pp. 223–250.

Supplementary Information:

Combined Spectroscopy and Electrical Characterization of La:BaSnO₃ Thin Films and Heterostructures

Arnaud P. Nono Tchiomo,^{1,2} Emanuela Carleschi,¹ Aletta R. E. Prinsloo,¹ Wilfried Sigle,³ Peter A. van Aken,³ Jochen Mannhart,³ Prosper Ngabonziza,^{1,3,a)} Bryan P. Doyle,^{1,b)}

¹*Department of Physics, University of Johannesburg, P.O. Box 524, Auckland Park 2006, Johannesburg, South Africa*

²*Van der Waals-Zeeman Institute, Institute of Physics, Science Park 904, 1098 XH Amsterdam, The Netherlands*

³*Max Planck Institute for Solid State Research, Heisenbergstr. 1, 70569 Stuttgart, Germany*

S1: Electronic Transport Measurements and Microstructural Characterizations

All La:BaSnO₃ samples were grown by pulsed laser deposition at an optimal target-substrate distance of 56 mm. The deposition parameters are given in Table I. After growth of La:BaSnO₃ films, Au/Ti contacts (45 nm thick) that provide electrical connections to the sample were added to the samples' corners using standard photolithography methods [Fig. S1(a)]. Basic electrical characterizations of the samples were performed using a physical property measurement system (PPMS) in four-point configuration with an excitation current of 1 μ A.

The scanning transmission electron microscopy (STEM) and electron energy loss spectroscopy (EELS) investigations were performed using a Cs-probe-corrected JEOL JEM-ARM200F. The EELS measurements were performed on the cross-section of BaSnO₃ buffered samples, and the electron beam was focused on the buffer layer and the La:BaSnO₃ film layer regions. Spectra from areas without and with La could then be compared, to see whether the doping alters or changes the oxidation state of the Sn.

In epitaxial thin film growth, a buffer layer can be employed to boost both the structural and electronic properties

TABLE I. Growth parameters of the La:BaSnO₃ thin films discussed in this study.

Sample	Thin film layer	Substrate	Deposition temperature (°C)	O ₂ partial pressure (mbar)	Laser fluence (J · cm ⁻²)	Laser repetition rate (Hz)
A	BaSnO ₃ (100 nm)	DyScO ₃	850	1.00 × 10 ⁻¹	1.5	4
	6% La:BaSnO ₃ (25 nm)		850	1.00 × 10 ⁻¹	1.5	1
B	BaSnO ₃ (100 nm)	TbScO ₃	850	1.00 × 10 ⁻¹	1.5	5
	6% La:BaSnO ₃ (25 nm)		850	1.00 × 10 ⁻¹	1.5	5
C	6% La:BaSnO ₃ (25 nm)	SrTiO ₃	850	1.05 × 10 ⁻¹	1.5	1
D	2% La:BaSnO ₃ (25 nm)	TbScO ₃	850	1.05 × 10 ⁻¹	1.5	1
E	BaSnO ₃ (25 nm)	SrTiO ₃	850	1.33 × 10 ⁻¹	1.5	1
	4% La:BaSnO ₃ (100 nm)		850	1.33 × 10 ⁻¹	1.5	1

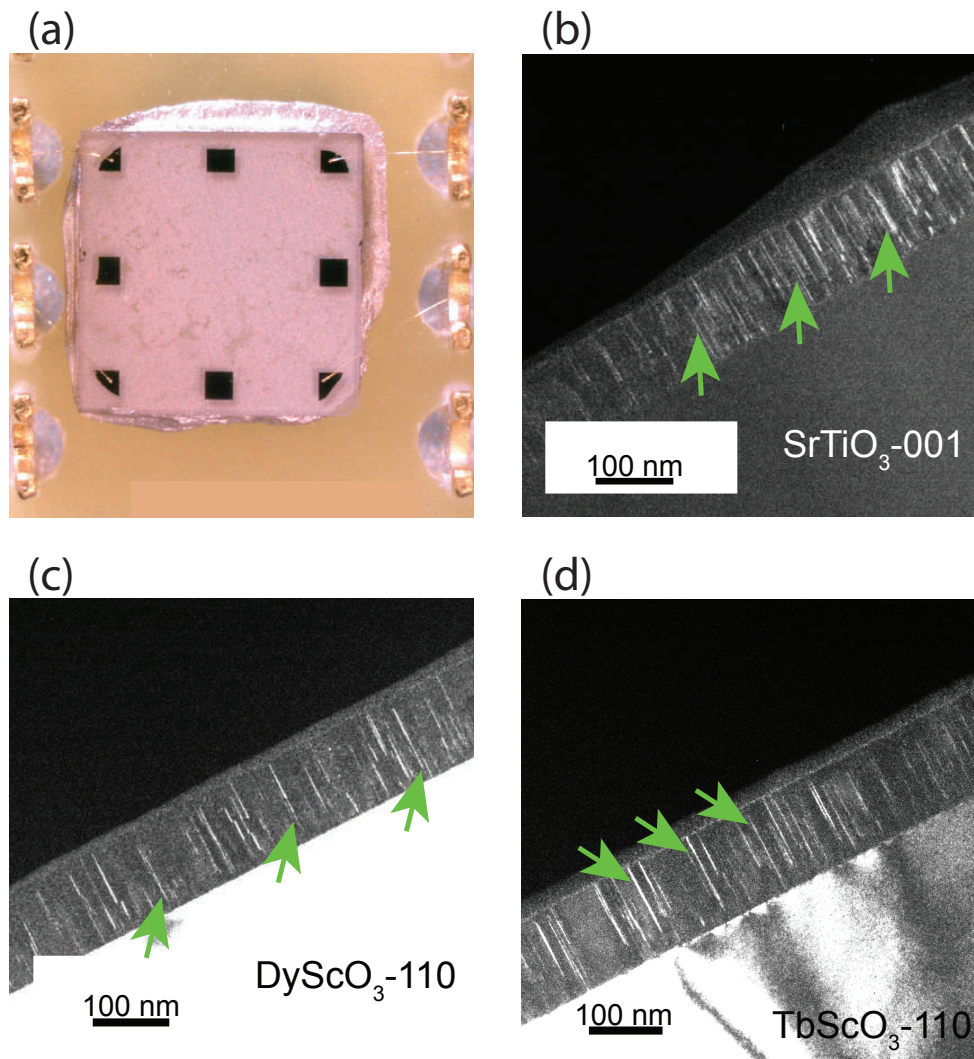


FIG. S1. (a) Optical photograph of a typical La:BaSnO₃ film structured in the Van der Pauw geometry, using metal contact pads of Au/Ti. The contacts are connected to the sample holder pins using aluminum wires bonded at the corners of the sample. (b) - (d) WB-DFTEM micrographs of (b) BaSnO₃/SrTiO₃, (c) BaSnO₃/DyScO₃ and (d) BaSnO₃/TbScO₃ heterostructures, showing threading dislocations (vertical bright contrasts) running across the film from the interface and represented by green arrows.

of the film [1, 2, 3]. The primary role of this additional layer is to reduce the density of defects, and in particular, the concentration of threading dislocations, which result in carrier density and carrier mobility reduction [1, 2, 3]. These dislocations are known to originate from misfit dislocations, which are generated at the film/substrate interface due to the large lattice mismatch between the as-deposited film layer and the substrate [4, 5, 6]. Figures S1(b)-(d) depict scanning transmission electron microscopy (STEM) micrographs of BaSnO₃/SrTiO₃, BaSnO₃/DyScO₃ and BaSnO₃/TbScO₃ heterostructures. Dense edge-type threading dislocations identified as vertical lines running across the film from the interface can be observed [4, 6]. A quantitative analysis of these threading dislocations carried out by counting the number of lines in 500 nm by 16 nm thick specimens gives a dislocation density of $10 \times 10^{11} \text{ cm}^{-2}$ in the film prepared on SrTiO₃, and $5 \times 10^{11} \text{ cm}^{-2}$ in the films grown with DyScO₃ and TbScO₃ substrates. This high concentration of threading dislocations acts as charge traps, and was reported to be responsible for the low activation rate of the carrier, as well as for the limitation of the electron mobility in La:doped BaSnO₃ systems [1, 7, 8].

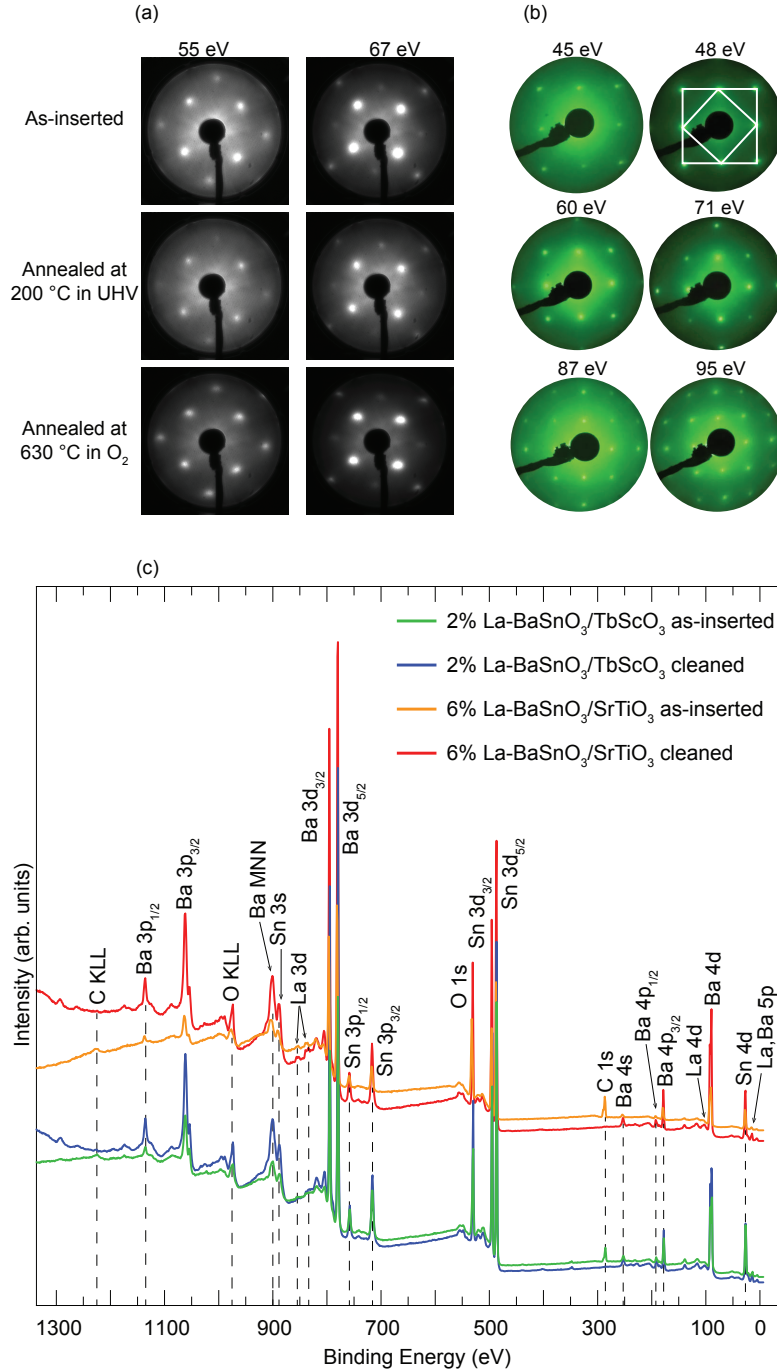


FIG. S2. (a) and (b) Representative LEED images from the surface of a La:BaSnO₃ (25 nm)/BaSnO₃ (100 nm)/TbScO₃ heterostructure. (a) The images are taken at various electron energies on the surface at different stages of cleaning. (b) The images are taken at various electron energies on the clean surface. The white squares drawn on the image recorded at 48 eV illustrate the square lattice of BaSnO₃. Note that at the electron energy of 48 eV, the diffraction pattern shows only first order beams, and when the energy is approximately doubled (at 95 eV), second order spots are observed. (c) XPS survey scans for as-inserted (light green and orange curves) and cleaned (blue and red curves) for the samples E and D. All the core levels from La, Ba, Sn and O elements can be seen in the spectra. The C 1s signal originating from surface contamination with the associated C KLL Auger electron peak are also visible. The spectra were acquired with an experimental resolution of 0.90 eV using the Al K_α excitation source.

S2: Photoemission Spectroscopy Measurements

The La:BaSnO₃ thin films and heterostructures were grown using pulsed laser deposition at the Max Planck Institute for Solid State Research, Stuttgart Germany. After electronic transport characterizations, samples were transported in ambient conditions to the University of Johannesburg in South Africa for further spectroscopic measurements. X-ray photoemission spectroscopy (XPS) and angle resolved photoemission spectroscopy (ARPES) spectra were collected using a SPECS PHOIBOS 150 hemispherical electron energy analyzer. The base pressure in the analysis chamber during acquisition of the core and valence XPS data was $\approx 3 \times 10^{-10}$ mbar. These were measured using monochromatized Al K_α and Ag L_α excitation sources, emitting photons of energies of 1486.71 eV and 2984.31 eV, respectively. The experimental resolutions with these two sources were 580 and 960 meV, respectively. To investigate the electronic band structure, we also excited the valence electrons of the samples using a He I source delivering photons of 21.2 eV. For these ARPES measurements, the experimental resolution was 120 meV.

As the samples had been exposed to air under ambient conditions, their surfaces were thoroughly cleaned in vacuum prior to spectroscopic measurements. The cleaning procedure consisted of annealing in O₂ environment at the temperature of ~ 700 °C in a preparation chamber maintained at $\approx 7 \times 10^{-6}$ mbar. The annealing procedure consisted of several cycles of 2 hours each and it was done using an e-beam heater at a maximum electron emission

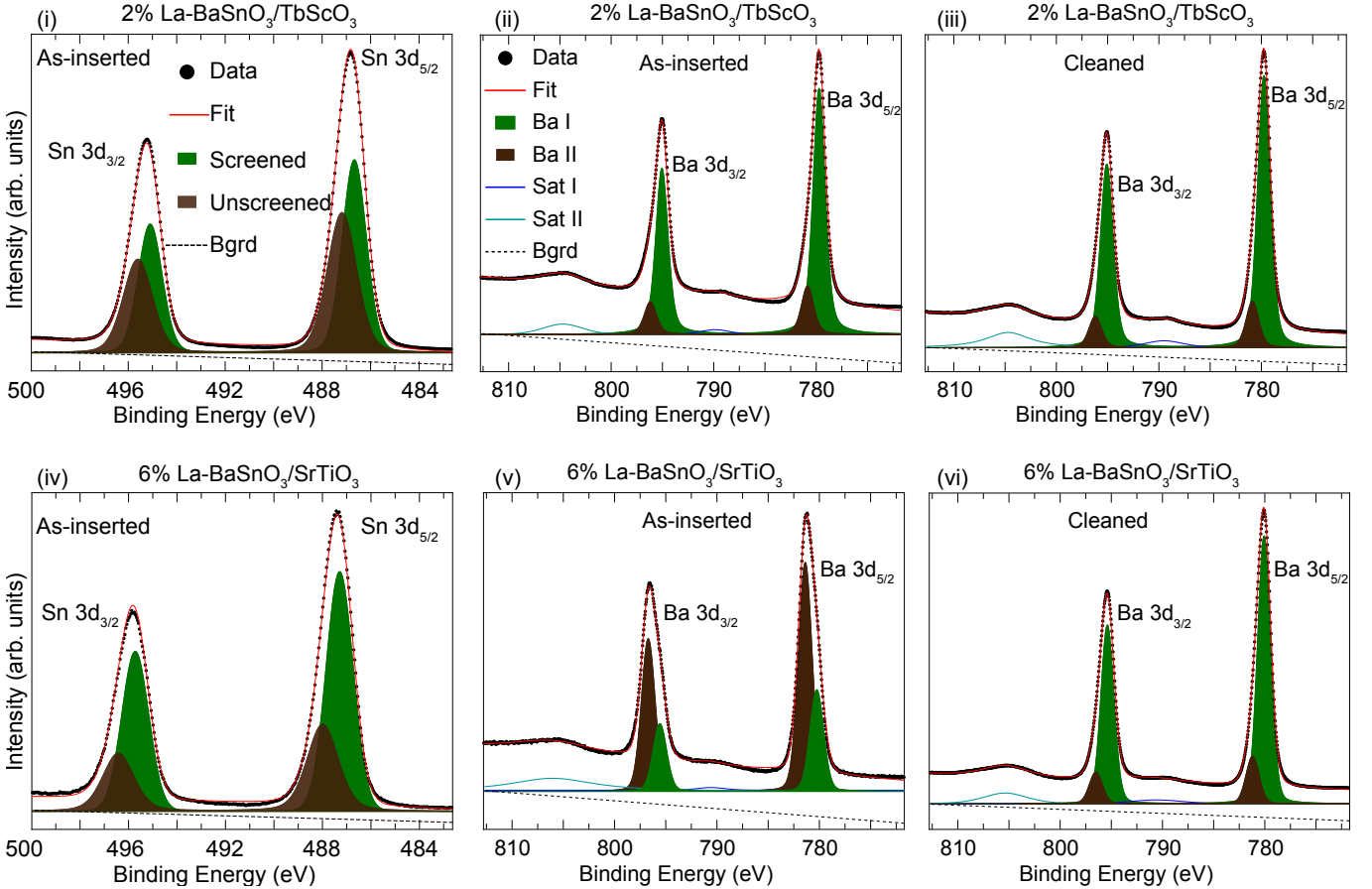


FIG. S3. Fits of the XPS spectra around the Sn 3d and Ba 3d regions for as-inserted and cleaned samples D (i-iii) and C (iv-vi), discussed in the main text. The spectra were fitted with two Voigt doublets. The data were acquired with an experimental resolution of 0.78 eV

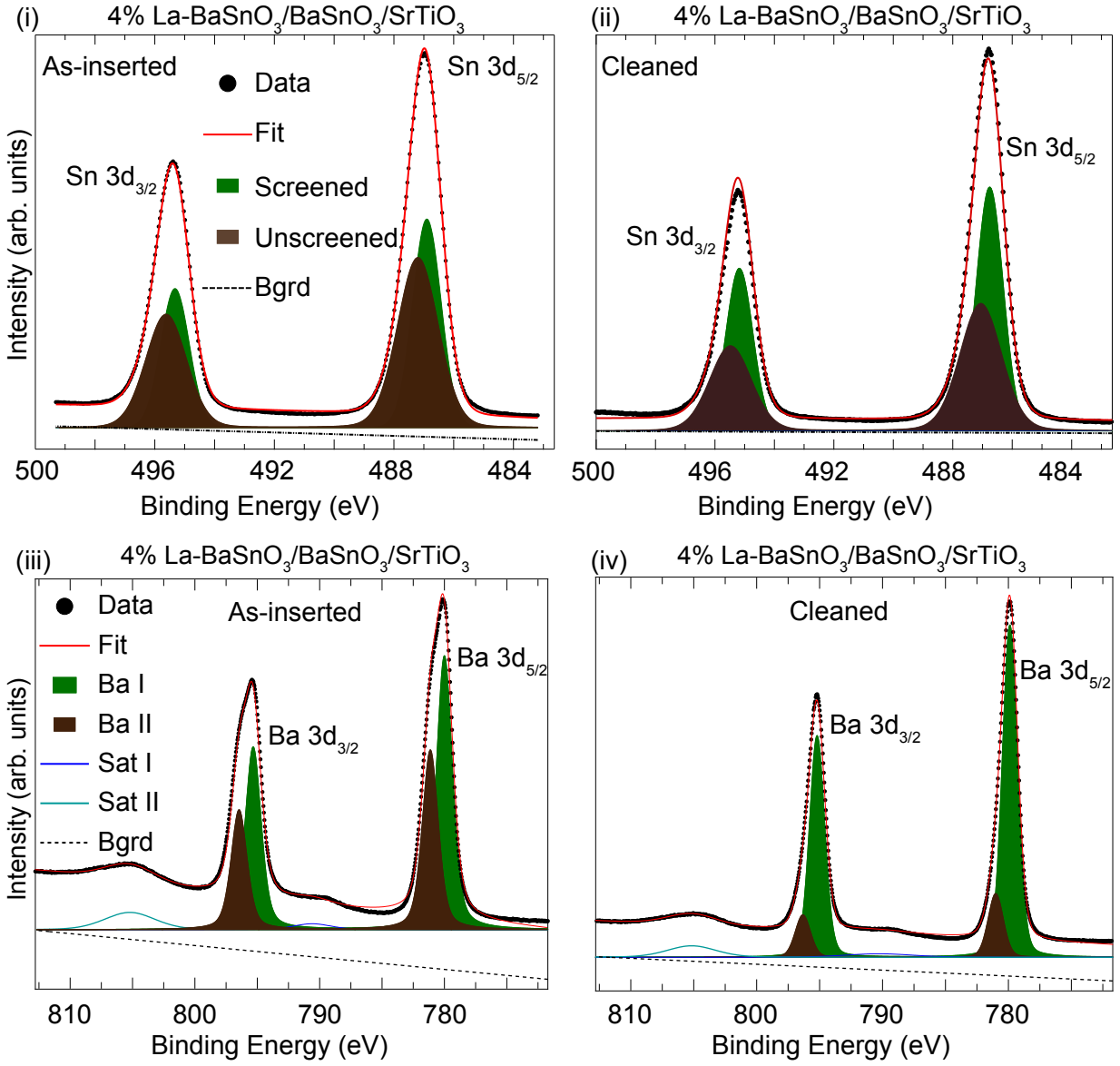


FIG. S4. Fits of the as-inserted and cleaned Sn 3d and Ba 3d XPS spectra for sample E.

power of 3.5 W. The temperature was indicated by a pyrometer set to an emissivity of 0.1. The cleanliness of the samples was monitored by recording the low-energy electron diffraction (LEED) patterns (to inspect the surface structure) directly after an annealing cycle [Fig. S2(a)], as well as by tracking the C 1s signal in the XPS survey scans [Fig. S2(c)] and by tracking the O 1s, Sn 3d and Ba 3d levels before and after surface cleaning [see, Fig. S3, Fig. S5]. LEED was also used for the determination of the orientation of the surfaces before ARPES measurements. Figure S2(a) and Fig. S2(b) depict representative LEED images of the La:BaSnO₃ (001) surface at different stages in the high-temperature cleaning process, and at different electron energies (clean surface), respectively.

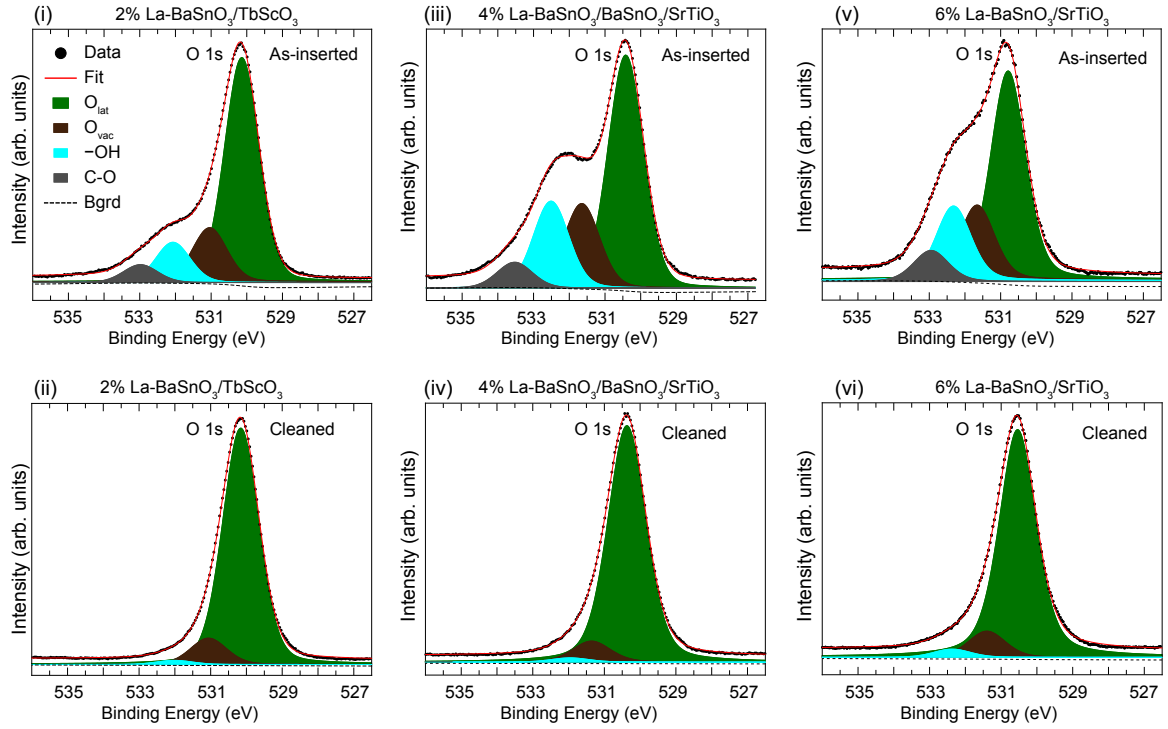


FIG. S5. Fits of the XPS spectra for the O 1s core levels for samples D (i and ii), E (iii and iv) and C (v and vi). The O 1s core electrons were fitted with four Voigt singlet components before cleaning, whereas three were used after vacuum cleaning steps. O_{lat} is the main component attributed to lattice oxygen. The peak labeled O_{vac} is a surface oxygen vacancy. This peak represents the change in the local electronic density of the other lattice oxygen atoms when an oxygen is removed [9, 10, 11]. $-\text{OH}$ and C-O are contamination related components, associated with adsorbed oxygen atoms resulting from the dissociation of water on the surface [12, 13, 14], and oxygen attached to organic residues or carbonates [13, 14], respectively.

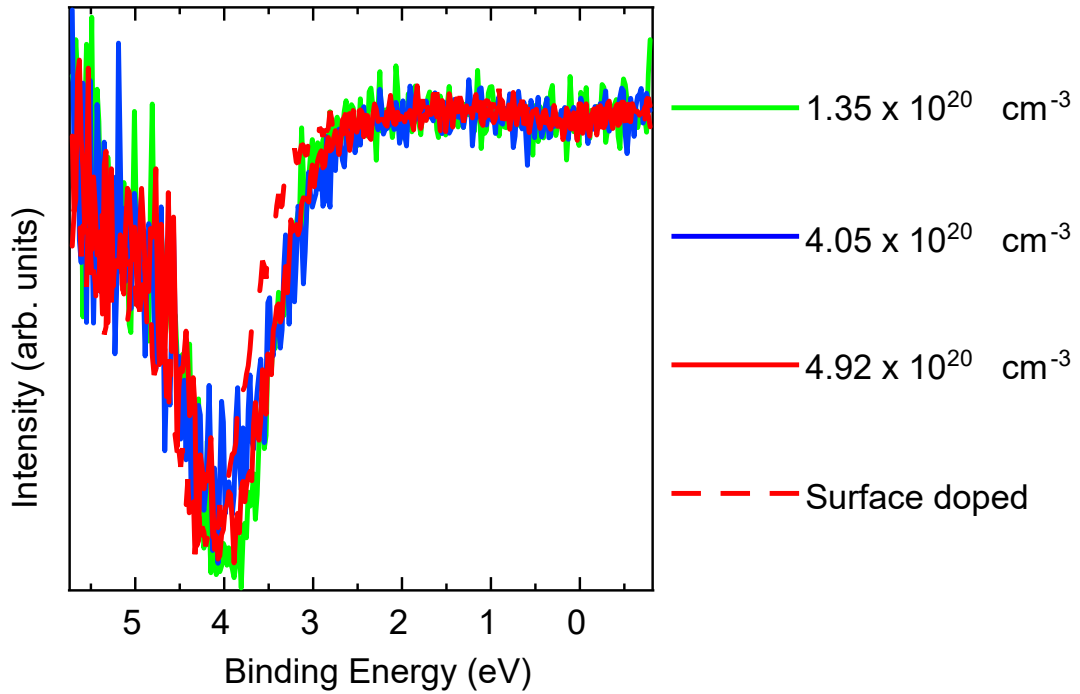


FIG. S6. First derivative of the XPS spectra discussed in Fig. 5 of the main text.

References

- [1] A. P. Nono Tchiomo, W. Braun, B. P. Doyle, W. Sigle, P. van Aken, J. Mannhart, and P. Ngabonziza, *APL Mater.* **7**, 041119 (2019).
- [2] S. Nakamura, *Jpn. J. Appl. Phys.* **30**, L1705 (1991).
- [3] Y. Huang, X. D. Chen, S. Fung, C. D. Beling, C. C. Ling, Z. F. Wei, S. J. Xu, and C. Y. Zhi, *J. Appl. Phys.* **96**, 1120 (2004).
- [4] H. Paik, Z. Chen, E. Lochocki, H. Ariel Seidner, A. Verma, N. Tanen, J. Park, M. Uchida, S. Shang, B. C. Zhou, M. Brützmam, R. Uecker, Z. K. Liu, D. Jena, K. M. Shen, D. A. Muller, and D. G. Schlom, *APL Mater.* **5**, 116107 (2017).
- [5] S. Raghavan, T. Schumann, H. Kim, J. Y. Zhang, T. A. Cain, and S. Stemmer, *APL Mater.* **4**, 016106 (2016).
- [6] J. Shiogai, K. Nishihara, K. Sato, and A. Tsukazaki, *AIP Adv.* **6**, 065305 (2016).
- [7] Z. Lebens-Higgins, D. O. Scanlon, H. Paik, S. Sallis, Y. Nie, M. Uchida, N. F. Quackenbush, M. J. Wahila, G. E. Sterbinsky, D. A. Arena, J. C. Woicik, D. G. Schlom, and L. F. Piper, *Phys. Rev. Lett.* **116**, 027602 (2016).
- [8] H. J. Kim, U. Kim, T. H. Kim, J. Kim, H. M. Kim, B. G. Jeon, W. J. Lee, H. S. Mun, K. T. Hong, J. Yu, K. Char, and K. H. Kim, *Phys. Rev. B* **86**, 165205 (2012).
- [9] M. Sirena, N. Haberkorn, M. Granada, L. B. Steren, and J. Guimpel, *J. Appl. Phys.* **105**, 033902 (2009).
- [10] J. Rubio-Zuazo, L. Onandia, P. Ferrer, and G. R. Castro, *Appl. Phys. Lett.* **104**, 021604 (2014).
- [11] K. Wang, Y. Ma, and K. Betzler, *Phys. Rev. B* **76**, 144431 (2007).
- [12] A. Fujishima, X. Zhang, and D. A. Tryk, *Surf. Sci. Rep.* **63**, 515 (2008).
- [13] J. C. Yu, J. Yu, H. Y. Tanga, and L. Zhang, *J. Mater. Chem.* **12**, 81 (2002).
- [14] J. Zhuang, S. Weng, W. Dai, P. Liu, and Q. Liu, *J. Phys. Chem. C* **116**, 25354 (2012).
- [15] G. Greczynski, and L. Hultman, *Prog. Mater. Sci.* **107**, 100591 (2020).
- [16] E. Korin, N. Froumin, and S. Cohen, *ACS Biomater. Sci. Eng.* **3**, 882 (2017).
- [17] D. Cabrera-German, G. Gomez-Sosa, and A. Herrera-Gomez, *Surf. Interface Anal.* **48**, 252 (2016).